Time-domain signal averaging to improve microparticles detection and enumeration accuracy in a microfluidic impedance cytometer

Brandon K. Ashley[1] and Umer Hassan[*123]

1. Department of Biomedical Engineering, Rutgers, the State University of New Jersey, Piscataway, NJ, 08854, USA.

2. Department of Electrical and Computer Engineering, Rutgers, the State University of New Jersey, Piscataway, NJ, 08854, USA.

3. Global Health Institute, Rutgers, the State University of New Jersey, New Brunswick, NJ, 08901, USA.

Emails: brandon.ashley@rutgers.edu, umer.hassan@rutgers.edu

** Corresponding Author: Tel (848) 445-2164*

ABSTRACT

Microfluidic impedance cytometry is a powerful system to measure micro and nano-sized particles and is routinely used in point-of-care settings disease diagnostics and other biomedical applications. However, small objects near a sensor's detection limit are plagued with relatively significant background noise and are difficult to identify for every case. While many data processing techniques can be utilized to reduce noise and improve signal quality, frequently they are still inadequate to push sensor detection limits. Here, we report the first demonstration of a novel signal averaging algorithm effective in noise reduction of microfluidic impedance cytometry data, improving enumeration accuracy and reducing detection limits. Our device uses a 22 μm tall by 100 μm wide (with 30 μm wide focused aperture) microchannel and gold coplanar microelectrodes that generates an electric field, recording bipolar pulses from polystyrene microparticles flowing through the channel. In addition to outlining a modified moving signal averaging technique theoretically and with a model dataset, we also performed a compendium of characterization experiments including variations in flow rate, input voltage, and particle size. Multi-variate metrics from each experiment are compared including signal amplitude, pulse width, background noise, and signal-to-noise ratio (SNR). Incorporating our technique resulted in improved SNR and counting accuracy across all experiments conducted, and the limit of detection improved from 5 μm to 1 μm particles without modifying microchannel dimensions. Succeeding this, we envision implementing our modified moving average technique to develop next generation microfluidic impedance cytometry devices with an expanded dynamic range and improved enumeration accuracy. This can be exceedingly useful for many biomedical applications, such as infectious disease diagnostics where devices may enumerate larger-scale immune cells alongside sub-micron bacterium in the same sample.

KEYWORDS: Microfluidics, signal processing, disease diagnostics, point-of-care

INTRODUCTION

Detecting micro and nano-sized objects has been widely explored over the last 70 years and is critical for many disciplines including medical diagnostics (Clausen et al., 2018; Evander et al., 2013; U. Hassan et al., 2017; U. Hassan & Bashir, 2014), environmental protection (Carminati et al., 2014; Ciccarella et al., 2016; Guo et al., 2015), and other industries (Bredar et al., 2020; Shi et al., 2021; Teass et al., 1998; Xu et al., 2016; Zhang et al., 2021). To accomplish this, one of the most common and promising methods may be electrochemical impedance spectroscopy (EIS) which measures the electrical properties of objects in response to an electric potential. While numerous configurations have been researched and implemented, typically this consists of bonded electrodes to generate an electric field on the surface of microchannels that facilitate microfluidic flow. EIS has many advantages over other micro-scale detection options, including a diversity of materials which can be measured (e.g., proteins (Baraket et al., 2017; Mok et al., 2014; Panneer Selvam & Prasad, 2017), immune cells (U. Hassan et al., 2017; Watkins et al., 2013), pathogens (Lam et al., 2013), particulate matter (Carminati et al., 2014; Ciccarella et al., 2016), and more (Guo et al., 2015; Shi et al., 2021; Teass et al., 1998; Zhang et al., 2021)), label-free detection capabilities, requiring small sample volumes, relatively inexpensive fabrication options, and the multiplexing ability to quantify many different materials altogether (Ashley & Hassan, 2021; Prakash et al., 2020). Additionally, at low voltages the detection process is non-destructive to sample analytes, and many EIS systems can be performed without manual sample pre-processing (Baraket et al., 2017; U. Hassan et al., 2017, p. 64). A powerful tool, EIS or more specifically microfluidic impedance cytometry (MIC) is continuing to make improvements in micro-sized object detection with innovations in fabrication methods and post-data collection digital processing.

A substantial bottleneck MIC and other micro-scale detection sources deal with are limits of the detection resolution. Indeed, the ability to measure smaller materials opens various pathways to greater sample understanding and measurement versatility. Currently, there is a balance between fabrication complexity, sensing dimensions, and external signal acquisition factors with the MIC accuracy and limit of detection. For example, materials such as proteins, antibodies, and DNA have been measured using MIC for a few decades now and can be detected with a relatively simple to fabricate device (Saleh & Sohn, 2003). However, in doing so the sensing region has a limiting dimension of 1 μm, and such a scheme is unable to simultaneously measure objects larger than that. Even objects near that aperture would have high clogging susceptibility and thus poor device quality control at that scale. To extend the dynamic range for MIC, an optimized balance must be achieved along with techniques that can reduce background noise from existing systems.

Simple strategies to reduce noise include digital signal processing after data collection. Many such approaches are already employed in MIC to remove baseline drift and other noise-dominating frequency regimes (U. Hassan et al., 2015; X. Liu et al., 2014; T. Sun et al., 2007). By only reducing noise in frequency alone, many noise contributions are neglected, and signal quality can remain inadequate especially as a majority of data points collected represent background noise. One technique yet to be coupled with time-domain MIC is common signal averaging (CSA), which is the principle that noise is random and when data points averaged together will reduce to smaller values relative to desired signal, improving signal quality (Umer Hassan & Anwar, 2010). CSA has been employed with many periodic electrical signal collection schemes such as electrocardiography (Kamath et al., 2011) and pulse oximetry (Janssens et al., 2011; Sukor et al., 2011), as well as superimposed image averaging in optical coherence tomography (Baumann et al., 2019; Berger et al., 2014) and even robotic stabilization (Balara et al., 2018; Khurana & Nagla, 2018). For these cases, however, the signal must occur at a consistent defined period, and the total data points are subdivided by the number of samples averaged at once. As is, it would be difficult to translate CSA to MIC since detected object incidences are random and the relative pulse data points are few, which may lose temporal resolution if total data points must be empirically subdivided.

Given the unique non-periodic nature of MIC data, we investigated and found that the moving average algorithm will be the most suitable signal averaging technique to be used. Here, rather than subdividing the data during averaging, an average is taken at the beginning of the next original data point, which levels off high variance data. The result is a data sparring signal processing technique that does not sacrifice on noise reduction potential. This interdisciplinary technique has been used in some biomedical (Chen et al., 2006; Manikandan & Soman, 2012) and robotic (Redhyka et al., 2015) applications, but is primarily utilized to predict stock market trends (de Souza et al., 2018; Ellis & Parbery, 2005; Metghalchi et al., 2012). Many moving average iterations exist (Vandewalle et al., 1999), but we focused on simple moving averaging (SMA) in this study, which averages each data point with equal weight and has the highest retention of original dataset properties. SMA may provide a simple and quick approach to reduce noise and improve detection limits without disrupting the balance of fabrication, sensitivity, and design complexity.

Here, we present a MIC device (Fig. 1a) coupled with a modified SMA algorithm to reduce background noise in time-domain data. Polystyrene (PS) microparticles are measured in a microfluidic channel with dual-grounded gold electrodes (Fig. 1b) that form a bipolar pulse when the middle electrode is voltage stimulated and forms an electric field (Fig. S1). This signal is improved using channel focusing regions (Fig. 1c) which increase PS particle amplitude. With this method, 1 µm PS particles are indistinguishable from background noise (Fig. 1d), but after applying our modified SMA technique to the same dataset, noise is significantly reduced and these particles can be qualitatively identified from their bipolar amplitudes (Fig. 1e). These properties can also be quantified based on noise variance, signal amplitude, and their relative signal-to-noise ratio (SNR). After defining mathematically, the principles of SMA and modelling its behavior, experiments were conducted with varying flow rates, input voltage, and particle sizes to characterize SMA effects and determine its potential to improve the sensor accuracy and limit of detection. To the best of our knowledge, this is the first demonstration of signal averaging used with MIC, or with random-incidence time-domain data of impedance-based detection.

MATERIALS AND METHODS

Gold electrode microfabrication

Gold electrodes were rendered by spin coating Microposit s1813 photoresist (Kayakuam, Tokyo, JPN) above a 4” borosilicate wafer (University Wafer, South Boston, MA, USA) at 3000 rpm, forming a 1.55 µm layer. After baking at 115°C for 60 seconds, the wafer is exposed to UV light at 150 mJ/cm^2 using a mask aligner and mask with rendered microelectrode design. The wafer is then submerged in Microposit MF-319 photodeveloper (Kayakuam, Tokyo, JPN) under slight agitation for 30 seconds or until features are visible. Wafers are submerged in hydrochloric acid for 45 minutes to etch glass in the electrode feature regions. After soft baking at 60°C for 15 minutes, the surface is treated with oxygen plasma. This is followed by 250 nm of chromium and 750 nm of gold sputtered above the s1813 photoresist. When submerging in acetone and under ultrasonic agitation, metal is removed except for the electrode regions through lift-off. A diamondbladed saw is then used to cut out individual electrode designs. The gold electrode fabrication process is depicted by Fig. S2.

For the final design, gold microelectrodes have a 100 µm width and are spaced 150 µm apart (Fig. 1b). Gold connection pads are fabricated with a 3 mm width.

Microfluidic channel fabrication and soft lithography

SU-8 3025 photoresist (Kayakuam, Tokyo, JPN) was spin-coated above a 4" silicon wafer (University Wafer, South Boston, MA, USA) at 4000 rpm, forming a 1.5 µm layer. After soft baking at 95°C for 5 minutes, the wafer is then exposed to UV light at 150 mJ/cm^2 using a mask aligner and mask to form the microfluidic channels. The wafer is rinsed with SU-8 developer (Kayakuam, Tokyo, JPN) for 4 minutes or until channel features are visible. After rinsing with isopropyl alcohol, the wafer is hard baked at 300°C for 30 minutes. The wafer surface is then treated with (3-Aminopropyl)triethoxysilane (Sigma Aldrich, St. Louis, MO, USA) to retain microchannel structure during soft lithography. Microchannel fabrication is detailed in Fig. S3.

Before soft lithography, polydimethylsiloxane (PDMS) is formed by combining 10 parts of Sylgard 184 elastomer base with 1 part curing agent (Dow, Midland, MI, USA). After thorough mixing, the solution is poured over channel features on the silicon wafer and cured at room temperature for 30 minutes under vacuum followed by baking at 60°C for 1 hour and at atmospheric pressure. Once cured, PDMS molds are cut and removed from the wafer with the embedded channel structures. A stereomicroscope is used to align and puncture inlet and outlet holes with a biopsy punch and PDMS channels are then cleaned with ethanol under sonic agitation for 45 minutes.

The final channel dimensions yield a 1 cm long channel that is 100 μm wide and 22 μm tall, with two focusing regions that reduce the width to 30 μm and has a 20 μm path length (Fig. 1c). Both focusing regions are spaced 280 μm between midpoints.

Device connections and equipment interfacing

The PDMS channel and gold electrodes are treated with oxygen plasma using a plasma chamber (100W power for 60 seconds at 60 cm^3 per min of oxygen under vacuum). Immediately after, the PDMS is aligned using a stereomicroscope and placed above the microelectrodes with focusing regions positioned between outer electrodes (Fig. 1c). After soft baking for 1 hour at 60°C, syringe tubing was inserted into PDMS inlet and outlet holes and syringe needles are inserted into the opposite end to facilitate media infusion using a syringe and the NE-300 syringe pump (Southpointe Surgical Supply, Coral Springs, FL, USA). Silver conductive epoxy components (Digi-Key Electronics, Thief River Falls, MN, USA) are combined to connect microfluidic devices with custom printed circuit boards (PCB, Sunstone Circuits, Mulino, OR, USA) and baked at 60°C for 1 hour. The PCB then connects with a custom Veroboard which facilitates transimpedance amplification for signal detection using HF2TA current amplifiers (Zurich Instruments, Zurich, SUI) from outer electrodes and inputs an AC voltage signal at a 303 kHz frequency to the middle electrode using a lock-in amplifier (Zurich Instruments, Zurich, SUI). PS particles (1, 3, 5, 7, and 9 μm diameters, 2.5% w/v, Spherotech, Lake Forest, IL, USA) are diluted in 1X phosphate buffered saline (PBS) and flow is driven through a syringe pump.

Signal acquisition, processing, and sampling algorithm

Signal acquisition process flow is outlined in the supplementary information (Fig. S4). First, current output from the device is converted to voltage and undergoes transimpedance amplification. The signal is further combined using a differential amplifier and data is stored at a 250 kHz sampling rate. A PCIe-6361 data acquisition card (16 bit, 2MB/s max) performs data recording, and all steps are managed on a LabView control program (National Instruments, Austin, TX, USA).

Subsequent digital filters are applied using MATLAB (version R2020B, MathWorks, Natick, MA, USA). A 4th order Butterworth filter is used for high (20 Hz cut-off) and low (100 kHz cut-off) pass filters, while a 1st order Butterworth filter is used for the band-stop filters to remove powerline interference (60 Hz and 120 Hz removed) using the Signal Processing Toolbox of MATLAB. See Fig. S5 for more detail.

After data collection and filtering (Fig. 1d), the MATLAB code then analyses and sets a threshold of values greater than 5 times the background noise to differentiate PS particle detection. Here, background noise (σ) is quantified as the root means squared of the first 5,000 data points.

$$\sigma = \sqrt{\frac{1}{m}\sum_i x_i^2} \tag{1}$$

Where m represents the number of data points and x is their respective voltage values. After defining a threshold, the bipolar amplitude for a particle (ΔV_T) is measured as the difference between the positive and negative peaks, collected as 1000 data points ± the threshold.

$$\Delta V_T = \Delta V_{max} - \Delta V_{min} \tag{2}$$

The algorithm stores each bipolar amplitude across the dataset. To ignore two or more PS particles flowing through the electric field at once, bipolar amplitudes are binned into 6 discrete categories, and the most common category is selected to represent bipolar amplitudes for one particle flowing through the channel ($\Delta V_{T,1PS}$) which normalizes the device sensitivity to only count 1 PS particle. The SNR is calculated based off this signal mode.

$$SNR = 20\log_{10}\left(\frac{\Delta V_{T,1PS}}{\sigma}\right) \tag{3}$$

Higher SNR indicates particles are better apparent, and an SNR greater than 20 is the cut-off for discernible sensing.

As a metric of particle transit time, the full width-half maximum (FWHM) was determined from particle pulses by measuring the number of data points greater than half the particle maximum value.

$$FWHM = \frac{m}{f_s}\ for\ x_i > \frac{\Delta V_{max}}{2} \tag{4}$$

Where m is the number data points (x_i) with a greater voltage value than half of ΔV_{max} for one particle pulse, and f_s is the device sampling rate set to 250 kHz. FWHM was measured and stored in MATLAB for only positive particle pulses.

Statistical evaluations

All studies evaluating significance between three or more groups was performed with a one-way ANOVA, with a null hypothesis of all group means are equal and alternative hypothesis of at least one group mean is unequal, and an α of 0.05. A Levene's test with all studies did not find significance, confirming homogeneity of variance, and a Tukey's post hoc test was conducted for studies which rejected the ANOVA null hypothesis. For studies comparing groups before and after signal averaging or only two groups, an unpaired T-test was conducted with a null hypothesis of the groups means being equal, an alternative hypothesis of the means being unequal, and an α of 0.05. Error bars displayed on figures represent one standard deviation away from the mean.

Signal averaging model

To validate our mathematical modelling as proof-of-concept, at first, a test dataset was generated in MATLAB featuring 200,000 data points of zeros followed by 200,000 data points of a simple waveform (i.e., sin(x)) with a sampling rate of 0.001 to model signal averaging trends (Fig. S6). Subsequently, White Gaussian noise was added to the signal using the awgn() function with a 12.3 SNR input using the Communications toolbox in MATLAB. Noise, bipolar amplitude, and SNR were calculated and were stored for increasing number of data points involved in sample averaging from 2 to 100. The technique and rationale behind the performed signal averaging method is dissected in the Theory section and implemented with this test dataset to reduce noise (Fig. S7).

THEORY

The most common signal averaging (CSA) method for physiological data averages an $\boldsymbol{n}$ number of data points from an original dataset (ODS) in series with $\boldsymbol{N}$ total data points, essentially subdividing the dataset by $\boldsymbol{n}$ (Umer Hassan & Anwar, 2010; Stupin et al., 2017):

$$CSA(i) = \frac{1}{n} \sum_{j=n(i-1)+1}^{ni} x_j \tag{5}$$

Where $\boldsymbol{n}$ represents the number of data points averaged together in the signal averaging technique, and $\boldsymbol{x}$ are the individual data points collected from the ODS. While computationally simple, CSA halves the dataset size for each $\boldsymbol{n}$ subdivision.

$$N_{CSA} = \frac{N_{ODS}}{n} \tag{6}$$

This makes it more susceptible to sample aliasing for average and high frequency data. Higher sampling rates can overcome this, but at the cost of massive dataset files which may not be viable in all environments. Additionally, resolution will degrade for metrics which function on the time domain (e.g., pulse width) that has proven useful in impedance cytometry determination (Feng et al., 2019; Norton et al., 2019; Prakash et al., 2020).

In contrast, signal averaging method applied for this work relies on a modified simple moving average (SMA) which deviates from CSA to preserve the number of data points while not sacrificing on noise reduction. With SMA, an average is taken from $\boldsymbol{n}$ data points and the next SMA value begins on the next ODS data point rather than the next data point not included in $\boldsymbol{n}$ like CSA.

$$SMA(i) = \frac{1}{n}\sum_{j=i}^{n+i-1} x_j \tag{7}$$

This is modified from a standard simple moving average as it starts with the first data point and selects succeeding points up until the selected signal averaging term $\boldsymbol{n}$, rather than starting with the last data point and working backwards (Vandewalle et al., 1999). Concurrently, the only data points lost are the last $\boldsymbol{n}$ values in the set.

$$N_{SMA} = N_{ODS} - n \tag{8}$$

While more signal averages must be computed versus CSA, the result is a resilient dataset to sample aliasing. SMA better suits impedance cytometry as object pulses happens rapidly (order of ms) and maximum intensity or pulse width data may be misrepresented from data point subdivisions.

The result from SMA leads to reductions in both bipolar amplitude and background noise but at different rates. If a dataset $x(k)$ is a function of both noise (x_{noise}) and desired signal (x_s), and has a f_s sampling rate:

$$x\left(\frac{k}{f_s}\right) = x_s\left(\frac{k}{f_s}\right) + x_{noise}\left(\frac{k}{f_s}\right) \tag{9}$$

Periodic signals that are statistically dependent with summate constructively and remain constant through $\boldsymbol{n}$ signal averaging.

$$\frac{1}{n}\sum_{j=1}^{n} x_{j,s}\left(\frac{k}{f_s}\right) = \frac{n}{n}x_{j,s}\left(\frac{k}{f_s}\right) = x_{j,s}\left(\frac{k}{f_s}\right) \tag{10}$$

Following this, Gaussian white noise is considered by assuming random and statistically independent values that inhabits the signal and with a zero average (μ_{noise}) after correcting for baseline drift (Marmarelis, 2004).

$$\mu_{noise} = 0 \tag{11}$$

Then averaging $\boldsymbol{n}$ number of data points will reduce noise at a characteristic rate based on standard deviation alone ($\boldsymbol{\sigma}$).

$$\frac{1}{n}\sum_{j=1}^{n} x_{j,noise}\left(\frac{k}{f_s}\right) = \frac{1}{n}\sqrt{n\sigma^2} = \frac{\sigma}{\sqrt{n}} \tag{12}$$

A relationship for SNR can then be predicted from the equation defined in the “Signal acquisition, processing, and sampling algorithm” section

$$SNR_{SMA} = 20\log_{10}\left(\frac{x_{j,s}\left(\frac{k}{f_s}\right)}{\sigma/\sqrt{n}}\right) = SNR_{ODS} + 20\log_{10}\left(\sqrt{n}\right) \tag{13}$$

SNR therefore increases with SMA assuming periodic signals and only Gaussian white noise.

RESULTS

Trends over the number of data points averaged together

Bipolar differential voltage amplitudes from 9 µm PS particles were recorded with our impedance cytometry device along with background noise measurements to determine the SNR without SMA. For the example experimental study, this included a 5V AC input voltage at 303 kHz and 15 µL/min flow rate. SMA was then performed with increasing number of signals averaged per iteration, from 2 to 100 data points averaged for each SMA data point. After measuring bipolar amplitudes, noise, and SNR for each SMA, we compared those values based on our model data and by directly following the equations derived in the Theory section. For all cases, starting values were normalized to the original experimental bipolar amplitude and noise to better visualize trends from SMA.

Fig. 2 graphs the changes in bipolar amplitude (Fig. 2a), noise (Fig. 2b), and SNR (Fig. 2c) with increasing number of data points averaged in the SMA algorithm following trends from the theoretical changes (dotted line), from our cyclic model data (dashed line) and from our experimental data (purple). For all cases, results closely follows the trend of noise reduction by the square root of the number of data points averaged together in forming the SMA data. Additionally, the model data only has a slight drop-off in bipolar amplitude after a few SMA iterations, but it decreases at a slower rate than noise, resulting in the SNR continuously improving with more SMA iterations. However, for our experimental data the bipolar amplitude from PS particles has a constant decrease in amplitude, to the degree that the rate of bipolar amplitude reduction exceeded noise reduction after a certain number of data points averaged in the SMA algorithm. This is visualized in Fig. 2c as an inflection point is reached in SNR at approximately 34 data points averaged to form the SMA model before SNR begins to decline with increasing data points averaged.

There are many reasons why the experimental data may fail to reach theoretical signal averaging potentials. One justification may be the presence of non-Gaussian pink noise in the experimental system even after filtering, as noise for experimental data does remain higher after SMA compared to the theoretical change and model changes (Antal et al., 2001) (Fig. 2b). Additionally, the theoretical trends are for synchronous, cyclic signals that are predicted to occur within the same period (Umer Hassan & Anwar, 2010). This remains apparent for the model, which were evaluating signals from a sine wave without changes in wavelength or breaks in waveform, and as such signal amplitude remained relatively steady. In the experiments, particle pulses are not periodic in occurrence and are more likely to have variations in pulse width from passing over the electric field at different heights. For heterogenous waveforms produced from PS particles to form the dataset, signal averaging is not perfectly constructive and is inversely proportional to the number of data points averaged. However, a degree of signal averaging markedly improves SNR up to a certain point, and for each experiment conducted some degree of signal averaging improved SNR.

In the following sections, mentions of results after SMA occur at the number of data points averaged that produced the highest SNR for that experiment. A compendium of the number of data points averaged together for the maximum SNR from each experiment is provided in Table S1.

Microfluidic flow rate optimizations

Experiments with different input flow rates were performed to optimize conditions for particle detection sensitivity, ensure counting accuracy, and observe trends from SMA for flow rate variations. Five different input flow rates were measured from 5 to 25 µL/min using 9 µm PS particles and an input voltage of 5 V with a 303 kHz AC frequency.

Fig. 3 details these results based on previous particle metrics such as PS bipolar amplitude (Fig. 3a), noise (Fig. 3b), and SNR (Fig. 3c). Here, there are no statistically significant ($p > 0.05$) differences between flow rates for bipolar amplitude, noise, or SNR between the original data and the data after applying the SMA algorithm. This indicates the variations in flow rates studied did not impact device performance, and all of them in their original form had an SNR of 26 dB or greater (Fig. 3c). However, there was significance for each flow rate when comparing each original dataset to their SMA counterpart for both bipolar amplitude, noise, and SNR ($p < 0.05$ for all cases), indicating the effects SMA has in improving SNR for each flow rate, which was now greater than 35 dB. While not a significant trend, there is a decline in maximum SNR with increasing flow rate after SMA. One justification for this may be a combination of slightly increased background noise from faster fluid flow (M. Liu & Franko, 2014) in the microfluidic channel through the sensing zone and less number of data points devoted to PS pulses as revealed by the decrease in FWHM with increasing flow rate (Fig. 3d). Indeed, signal pulses that have less data attributed to them may decline quicker from SMA, and this is confirmed as their maximum SNR was achieved with less data points averaged together than slower flow rates (Table S1). This also indicates the importance for adopting SMA versus CSA as CSA would more rapidly reduce the data points describing the PS pulses with the number of data points averaged and degrade their amplitude representation.

The change in transit time per particle and the number of particles counted per flow rate was also recorded to ensure accurate particle counting using our device. Fig. 3d reveals a decrease in FWHM per particle for increasing flow rates that is consistent with a 3rd power exponential decrease ($R^2 = 0.996$) as flow rate and average fluid velocity over the electric field have a cubic relationship based on Hagen-Poiseuille flow. Using a constant PS concentration of 40 particles/µL across each flow rate, there is a linear trend ($R^2 = 0.987$) in the number of particles counted per second (Fig. 3e). From this, the measured particle concentration is determined from each flow rate and it is found none of them statistically deviated from the given 40 particles/µL concentration ($p > 0.05$) and their means have a less than 10% error from the true concentration (Fig. 3f).

Variations in input voltage amplitude

Using 9 µm PS particles with a constant 15 µL/min flow rate, the effects of peak-to-peak input voltage were considered in relation to signal averaging. Here, the channel impedance has a direct relationship with input voltage magnitude (Daniels & Pourmand, 2007), and to a certain extent increased voltage input leads to greater signal prevalence above background noise with a constant voltage frequency. There are restrictions to input voltage however, as a linear range defining voltage and impedance is limited after small values (~less than 10 mV) and beyond this predicting impedance from input voltage is exceedingly difficult (Barbero et al., 2005). In many cases though, signal are orders of magnitude smaller than noise for input voltages less than 10 mV, and a lock-in amplification process is typically used to isolate signal data from noise based on specific frequency properties (Daniels & Pourmand, 2007; Talukder et al., 2017). In doing so however, the filtered noise is no longer Gaussian, being filtered out except for a small frequency range, making these situations incompatible for SMA. Additionally, the conditions for using a lock-in amplifier for frequency selection are not always feasible, and there are several previous reports which have found success using larger input voltages (~1–10 V) that maintain Gaussian noise (Caselli et al., 2021; Ciccarella et al., 2016; U. Hassan et al., 2017, p. 64; Wang et al., 2017). As such, this will be the input voltage regime assessed for this device.

PS particles were measured with varying input voltages of 0.5, 1, 5 and 10 V. Fig. 4 displays the changes in bipolar amplitude (Fig. 4a), background noise (Fig. 4b), and SNR (Fig. 4c) using these different input voltages. For the original data (dark gray), PS pulse bipolar amplitude and SNR increased for increasing input voltage (only comparing 1 and 5 V were statistically different), while noise remained relatively unchanged. After SMA for each input voltage (light gray), both bipolar amplitude and noise were reduced, but noise was reduced at a lower rate leading to a relative SNR increase. A logarithmic relationship is found for SNR with increasing input voltage for both the original data ($R^2 = 0.9882$) and after SMA ($R^2 = 0.9894$), which may be attributed to the nonlinear relationship between voltage and impedance in these high-voltage regimes (Barbero et al., 2005).

Representative PS pulses before (Fig. 4d) and after (Fig. 4e) SMA for each input voltage also reinforce relative noise reduction and greater particle detection, as the unnoticeable 0.5 and 1 V pulses (green and blue respectively) in the original data can be differentiated after SMA. This is further affirmed as SNR increased above 20 dB for both cases after SMA (Fig. 4c). Beyond qualitative evaluations for measuring pulses, the device was able to assess particle concentration more accurately from SMA. Fig. 4f reveals the number of particles detected as a function of increasing data points used in the SMA algorithm. Originally, particle counts were not close to the actual particle concentration of 160 particles/μL for the 0.5 and 1 V data. However, only after a few data points are averaged using SMA, true particles pulses are isolated from the noise and remain within 5% of the true concentration after using more data points in the SMA algorithm

(Table S2). This attests to the ability of SMA to improve particle detection from otherwise noisy data because of changes in input voltage and upgrade it to an accurate counting device.

Limit of detection analysis with PS particle size variations

To evaluate the limitations of this device coupled with SMA, PS particles with 1, 3, 5, 7, and 9 µm diameters were measured in separate solutions using a constant 5 V AC voltage input and a 15 µL/min flow rate. Fig. 5 illustrates these results, including metric changes discussed in previous sections such as changes in PS pulse amplitudes (Fig. 5a), noise (Fig. 5b), and SNR (Fig. 5c) for each PS size experiment. For the original data, increasing particle size led to an increase in bipolar amplitude, while noise remained statistically the same across different sizes ($p > 0.05$), which corresponds with a linear increase in SNR (maroon, $R^2 = 0.9871$). After SMA, again the bipolar amplitude and noise had characteristic magnitude reductions, which led to increased shifts in SNR. This is notable primarily for bringing the 1 and 3 µm particle solutions above the discernible 20 dB SNR threshold after SMA and likewise lowering the device's limit of detection (LOD). The changes in SNR after SMA for different particle sizes also had a linear trajectory (gray, $R^2 = 0.9703$), which is the combination of logarithmic changes in SNR for a typical linear increase in bipolar amplitude and the cubic increase in PS volume per linear diameter changes, as PS volume scales with displaced media in the channel detection regime and likewise a direct change in recorded impedance (Sui et al., 2020). This is supported by the cubic increase in bipolar amplitude relative to particle size shown in Fig. 5a. If this linear change in SNR holds across all particle sizes and if a 20 dB SNR is the benchmark for accurate detection, the device used in this study originally could only measure a 3.17 µm PS particle, but after SMA it may measure particles as small as 0.56 µm.

Fig. 5 also highlights select bipolar pulses from varying PS sizes before (Fig. 5d) and after (Fig. 5e) SMA. Originally, the 1 and 3 μm PS particles are difficult to recognize outside the noise band, and even larger particles such as 5 and 7 μm PS particles have an SNR near the discernible limit. However, after SMA the noise is significantly smoothed relative to PS pulses, and all PS waveforms are recognizable. Studies were also conducted related the number of data points averaged in the SMA algorithm to the particle concentration measured by the device (Fig. 5f). Similar to results from Fig. 4f, particle sizes originally near the 20 dB SNR detection limit were significantly lower in particle counts versus the true concentration of 300 particles/μL. However, performing SMA with increasing data points used led to the accurate counting of all particle sizes, with smaller particles requiring more SMA data points to reach 5% error of the actual concentration (Table S2). This shows the power SMA has with this device to improve both accurate counting of micron-sized particles and lower the LOD to measure smaller particles than originally determined.

DISCUSSION

In this research, a microfluidic impedance cytometry device was conceived, and its detection performance improved through digital signal processing with simple moving averaging; a technique implemented with this application for the first time. Here, white Gaussian noise is summed together destructively while consistent bipolar pulse signals are reduced at a slower rate. The result is data with relatively lower background noise which allows smaller particles to be detected and greater counting accuracy achieved. Likewise, it was demonstrated that SNR after SMA increased for each experiment iteration including experiments at different flow rates, with different input voltages, and for different sized PS particles. Another key takeaway is as we push the limit of MIC sensing (low flow rates, smaller particle sizes, and lower signal amplitudes), a greater number of data points averaged together are required in the SMA algorithm for achieving maximum SNR before the inflection point and SNR decline (Table S1).

The modified simple moving averaging method selected for this application comes with many considerations. For flow-based impedance detection in a microfluidic channel, a balance is struck for the flow rate that is slow enough to measure objects with sufficient temporal resolution but also fast enough to drive particles through the channel midpoint and reduce clogging in the low aspect-ratio channel dimensions (Dressaire & Sauret, 2017; Thompson et al., 2015). The compromise is a system with high sampling rates (200 kHz or greater) to adequately measure particles generating pulses in only a few milliseconds. One straightforward alternative may be to diminish the channel and detection cross section further, as particles in this system will contribute a greater impedance shift relative to flowing media and will have greater pulse amplitudes. However, this approach is limited from greater fabrication complexity, higher device failure from clogging, and cannot measure nondeformable objects larger than the channel dimensions. With applications directed towards heterogenous whole blood analysis, white blood cells may be as large as 15 μm in diameter, which is near the limits of our device detection dimensions already and could not consistently flow through a channel with smaller features. SMA allows for a modest post-processing approach to improve the LOD without redesigning the channel and sacrificing larger particle counting.

Since the data representing individual particle pulses is sparse, the averaging method must have high data point retention to avoid sample aliasing. The modified simple moving averaging technique fits these requirements, as detailed in Theory section, where the number of data points lost across the whole file is the number of data points averaged in the SMA algorithm. While even higher sampling rates may facilitate other signal averaging methods that subdivides the data, they come at the cost of exceedingly large original file sizes (~100s of MB) after only a few seconds of recording. This is unsatisfactory notably for common microfluidic impedance counting purposes such as point-of-care diagnostics (Ashley & Hassan, 2021). From using SMA in this report, processing time was increased on the order of minutes, totaling less than 10 minutes from sample collection to applying digital filters, SMA, and analyzing particle metrics. For MICs analyzing higher particle concentrations or for larger sample volumes to analyze, processing time and file sizes will proportionally increase. However, this is the case regardless of using SMA, and implementing SMA adds processing time that would not significantly hinder its application for general MIC use.

While the power of SMA has been presented with this impedance cytometry configuration, there are limitations which may prevent its ubiquitous translation with other devices or environments. Firstly, SMA can only characteristically reduce white Gaussian noise. Other digital signal processing mechanisms may alter background noise to persist in certain frequencies. Additionally, sources of pink noise like defects in the physical device materials and resistance fluctuations in component semiconductors are sometimes unavoidable, and pink noise will not reduce during SMA at the rate of white noise (Kogan, 2008; Weissman, 1988). It is not to say that SMA cannot improve signal quality under these conditions, but that the degree of change will be less drastic and less characterized. Another limitation is that SMA cannot distinguish competitive analyte species with similar pulse frequencies or exaggerate their amplitude differences, treating all objects which are counted with equal scrutiny. To better differentiate two or more materials, other phenotypic properties must be exploited (e.g., measure more electrically sensitive particles, probe particles at different input frequencies, or use functionalized particles for receptor attachment and identification) (Ashley et al., 2021; Prakash et al., 2020; Sui et al., 2020). Finally, the maximum SNR achieved would reach a climax and begin to decline from increasing number of data points used in the SMA algorithm. This was not consistent to the model periodic data or representative relationship equations, where SNR should continuously improve with the number of data points averaged together. Causes for this may include pulse amplitude and width variations, and pulse occurrences randomly happening, as signal averaging requires cyclic signals that have consistent occurrences to summate constructively. Though SNR did improve for each experiment using SMA, the number of data points used in the algorithm to reach the maximum SNR was less for original data that initially started with higher SNR's like the 5 or 10 V input voltage experiments (Table S1). This may be due a higher slope in the pulse waveform, and during averaging will smooth and flatten out at a faster rate for more data points relative to pulses with the same width having lower slopes. Similarly, faster flow rate SNRs explored in from flow rate variation experiments peaked with less data points averaged, but this is due to the smaller pulse width and fewer data points representing the pulse rather than a change in amplitude. Based on these conclusions, SMA may serve greater applications in identifying objects near the LOD threshold rather than further improving signal quality of already distinct signal.

For determining the optimal signal quality using SMA, the number of data points selected in the SMA algorithm is most critical. Ideally, an initial sweep should be performed similar to this report using an SMA with a varying number of data points averaged together to pinpoint the SNR inflection point. However, it may be estimated that detecting objects with an originally poor SNR will require a larger number of particles averaged together in the SMA algorithm (Table S1). This translated to smaller particles and with smaller input voltages with our design and dimensions. For systems with a poor SNR due to Gaussian noise, the maximum SNR achieved may be from 50–

100 data points used in the SMA algorithm, while a higher starting SNR may reach a maximum between 5–40 data points.

CONCLUSION

SMA may prove to be a versatile tool that can make MIC more flexible for different conditions. An improved LOD was shown for this device, and at the length-scales measured opportunities for more objects as small as individual bacterium may be measured with greater confidence. Other components could also be sacrificed in the face of certain conditions, such as low-input voltage requirements in point-of-care settings like battery or solar-powered devices (L. Liu & Choi, 2017; Montes-Cebrián et al., 2019; A. Sun et al., 2014; Yeh et al., 2017). Future studies will apply the characterizations determined in this report using SMA to objects beyond PS particles. Specifically, efforts will be made to ensure greater impedance-based counting accuracy of multiple immune cell biomarkers to determine pathophysiological conditions such as sepsis, cancer, HIV, or other difficult to diagnose diseases.

AUTHOR CONTRIBUTIONS

B.K.A. participated in: Data curation, formal analysis, funding acquisition, visualization, writing – original draft, writing – review & editing. U.H. participated in: Conceptualization, funding acquisition, investigation, project administration, resources, supervision, writing – review & editing.

CONFLICTS OF INTEREST

There are no conflicts to declare.

ACKNOWLEDGEMENTS

Authors would like to acknowledge the funding support from Department of Electrical and Computer Engineering, Global Health Institute at Rutgers, The State University of New Jersey and Rutgers VCRI Exploratory Research Grant. Authors also acknowledges support from NSF Award Number (2002511 and 2053149) and the National Institute of General Medical Sciences (NIGMS) as part of the National Institute of Health's (NIH) training grant T32 GM135141.

DATA Availability Statement

Data related to this study will be available upon request based on the funding agencies and Rutgers, The State University of New Jersey policies.

REFERENCES

Antal, T., Droz, M., Györgyi, G., & Rácz, Z. (2001). 1 / f Noise and Extreme Value Statistics. *Physical Review Letters*, *87*(24), 240601. https://doi.org/10.1103/PhysRevLett.87.240601

Ashley, B. K., & Hassan, U. (2021). Point-of-critical-care diagnostics for sepsis enabled by multiplexed micro and nanosensing technologies. *WIREs Nanomedicine and Nanobiotechnology*, *n/a*(n/a), e1701. https://doi.org/10.1002/wnan.1701

Ashley, B. K., Sui, J., Javanmard, M., & Hassan, U. (2021). Functionalization of hybrid surface microparticles for in vitro cellular antigen classification. *Analytical and Bioanalytical Chemistry*, *413*(2), 555–564. https://doi.org/10.1007/s00216-020-03026-4

Balara, M., Dupláková, D., & Matisková, D. (2018). Application of a signal averaging device in robotics. *Measurement*, *115*, 125–132. https://doi.org/10.1016/j.measurement.2017.10.037

Baraket, A., Lee, M., Zine, N., Sigaud, M., Bausells, J., & Errachid, A. (2017). A fully integrated electrochemical biosensor platform fabrication process for cytokines detection. *Biosensors and Bioelectronics*, *93*, 170–175. https://doi.org/10.1016/j.bios.2016.09.023

Barbero, G., Alexe-Ionescu, A. L., & Lelidis, I. (2005). Significance of small voltage in impedance spectroscopy measurements on electrolytic cells. *Journal of Applied Physics*, *98*(11), 113703. https://doi.org/10.1063/1.2137444

Baumann, B., Merkle, C. W., Leitgeb, R. A., Augustin, M., Wartak, A., Pircher, M., & Hitzenberger, C. K. (2019). Signal averaging improves signal-to-noise in OCT images: But which approach works best, and when? *Biomedical Optics Express*, *10*(11), 5755–5775. https://doi.org/10.1364/BOE.10.005755

Berger, A., Cavallero, S., Dominguez, E., Barbe, P., Simonutti, M., Sahel, J.-A., Sennlaub, F., Raoul, W., Paques, M., & Bemelmans, A.-P. (2014). Spectral-Domain Optical Coherence Tomography of the Rodent Eye: Highlighting Layers of the Outer Retina Using Signal Averaging and Comparison with Histology. *PLOS ONE*, *9*(5), e96494. https://doi.org/10.1371/journal.pone.0096494

Bredar, A. R. C., Chown, A. L., Burton, A. R., & Farnum, B. H. (2020). Electrochemical Impedance Spectroscopy of Metal Oxide Electrodes for Energy Applications. *ACS Applied Energy Materials*, *3*(1), 66–98. https://doi.org/10.1021/acsaem.9b01965

Carminati, M., Pedalà, L., Bianchi, E., Nason, F., Dubini, G., Cortelezzi, L., Ferrari, G., & Sampietro, M. (2014). Capacitive detection of micrometric airborne particulate matter for solid-state personal air quality monitors. *Sensors and Actuators A: Physical*, *219*, 80–87. https://doi.org/10.1016/j.sna.2014.09.003

Caselli, F., De Ninno, A., Reale, R., Businaro, L., & Bisegna, P. (2021). A Bayesian Approach for Coincidence Resolution in Microfluidic Impedance Cytometry. *IEEE Transactions on Biomedical Engineering*, *68*(1), 340–349. https://doi.org/10.1109/TBME.2020.2995364

Chen, S.-W., Chen, H.-C., & Chan, H.-L. (2006). A real-time QRS detection method based on moving-averaging incorporating with wavelet denoising. *Computer Methods and Programs in Biomedicine*, *82*(3), 187–195. https://doi.org/10.1016/j.cmpb.2005.11.012

Ciccarella, P., Carminati, M., Sampietro, M., & Ferrari, G. (2016). CMOS monolithic airborne-particulate-matter detector based on 32 capacitive sensors with a resolution of 65zF rms. *2016 IEEE International Solid-State Circuits Conference (ISSCC)*, 486–488. https://doi.org/10.1109/ISSCC.2016.7418119

Clausen, C. H., Dimaki, M., Bertelsen, C. V., Skands, G. E., Rodriguez-Trujillo, R., Thomsen, J. D., & Svendsen, W. E. (2018). Bacteria Detection and Differentiation Using Impedance Flow Cytometry. *Sensors (Basel, Switzerland)*, *18*(10). https://doi.org/10.3390/s18103496

Daniels, J. S., & Pourmand, N. (2007). Label-Free Impedance Biosensors: Opportunities and Challenges. *Electroanalysis*, *19*(12), 1239–1257. https://doi.org/10.1002/elan.200603855

de Souza, M. J. S., Ramos, D. G. F., Pena, M. G., Sobreiro, V. A., & Kimura, H. (2018). Examination of the profitability of technical analysis based on moving average strategies in BRICS. *Financial Innovation*, *4*(1), 3. https://doi.org/10.1186/s40854-018-0087-z

Dressaire, E., & Sauret, A. (2017). Clogging of microfluidic systems. *Soft Matter*, *13*(1), 37–48. https://doi.org/10.1039/C6SM01879C

Ellis, C. A., & Parbery, S. A. (2005). Is smarter better? A comparison of adaptive, and simple moving average trading strategies. *Research in International Business and Finance*, *19*(3), 399–411. https://doi.org/10.1016/j.ribaf.2004.12.009

Evander, M., J. Ricco, A., Morser, J., A. Kovacs, G. T., K. Leung, L. L., & Giovangrandi, L. (2013). Microfluidic impedance cytometer for platelet analysis. *Lab on a Chip*, *13*(4), 722–729. https://doi.org/10.1039/C2LC40896A

Feng, Y., Huang, L., Zhao, P., Liang, F., & Wang, W. (2019). A Microfluidic Device Integrating Impedance Flow Cytometry and Electric Impedance Spectroscopy for High-Efficiency Single-Cell Electrical Property Measurement. *Analytical Chemistry*, *91*(23), 15204–15212. https://doi.org/10.1021/acs.analchem.9b04083

Guo, Y., Liu, X., Sun, X., Cao, Y., & Wang, X. (2015). A PDMS Microfluidic Impedance Immunosensor for Sensitive Detection Of Pesticide Residues in Vegetable Real Samples. *Int. J. Electrochem. Sci.*, *10*, 10.

Hassan, U., & Bashir, R. (2014). Coincidence detection of heterogeneous cell populations from whole blood with coplanar electrodes in a microfluidic impedance cytometer. *Lab on a Chip*, *14*(22), 4370–4381. https://doi.org/10.1039/C4LC00879K

Hassan, U., Ghonge, T., Jr, B. R., Patel, M., Rappleye, M., Taneja, I., Tanna, A., Healey, R., Manusry, N., Price, Z., Jensen, T., Berger, J., Hasnain, A., Flaugher, E., Liu, S., Davis, B., Kumar, J., White, K., & Bashir, R. (2017). A point-of-care microfluidic biochip for quantification of CD64 expression from whole blood for sepsis stratification. *Nature Communications*, *8*(1), 15949. https://doi.org/10.1038/ncomms15949

Hassan, U., Reddy, B., Damhorst, G., Sonoiki, O., Ghonge, T., Yang, C., & Bashir, R. (2015). A microfluidic biochip for complete blood cell counts at the point-of-care. *TECHNOLOGY*, *03*(04), 201–213. https://doi.org/10.1142/S2339547815500090

Hassan, Umer, & Anwar, M. S. (2010). Reducing noise by repetition: Introduction to signal averaging. *European Journal of Physics*, *31*(3), 453–465. https://doi.org/10.1088/0143-0807/31/3/003

Janssens, J.-P., Borel, J.-C., Pépin, J.-L., & Group, on behalf of the S. (2011). Nocturnal monitoring of home non-invasive ventilation: The contribution of simple tools such as pulse oximetry, capnography, built-in ventilator software and autonomic markers of sleep fragmentation. *Thorax*, *66*(5), 438–445. https://doi.org/10.1136/thx.2010.139782

Kamath, G. S., Zareba, W., Delaney, J., Koneru, J. N., McKenna, W., Gear, K., Polonsky, S., Sherrill, D., Bluemke, D., Marcus, F., & Steinberg, J. S. (2011). Value of the signal-averaged electrocardiogram in arrhythmogenic right ventricular cardiomyopathy/dysplasia. *Heart Rhythm*, *8*(2), 256–262. https://doi.org/10.1016/j.hrthm.2010.10.007

Khurana, A., & Nagla, K. S. (2018). Signal Averaging for Noise Reduction in Mobile Robot 3D Measurement System. *MAPAN*, *33*(1), 33–41. https://doi.org/10.1007/s12647-017-0236-2

Kogan, S. (2008). *Electronic Noise and Fluctuations in Solids*. Cambridge University Press.

Lam, B., Das, J., Holmes, R. D., Live, L., Sage, A., Sargent, E. H., & Kelley, S. O. (2013). Solution-based circuits enable rapid and multiplexed pathogen detection. *Nature Communications*, *4*(1), 2001. https://doi.org/10.1038/ncomms3001

Liu, L., & Choi, S. (2017). Self-sustainable, high-power-density bio-solar cells for lab-on-a-chip applications. *Lab on a Chip*, *17*(22), 3817–3825. https://doi.org/10.1039/C7LC00941K

Liu, M., & Franko, M. (2014). Influences of Detection Pinhole and Sample Flow on Thermal Lens Detection in Microfluidic Systems. *International Journal of Thermophysics*, *35*(12), 2178–2186. https://doi.org/10.1007/s10765-014-1714-1

Liu, X., Li, L., & Mason, A. J. (2014). High-throughput impedance spectroscopy biosensor array chip. *Philosophical Transactions of the Royal Society A: Mathematical, Physical and Engineering Sciences*, *372*(2012), 20130107. https://doi.org/10.1098/rsta.2013.0107

Manikandan, M. S., & Soman, K. P. (2012). A novel method for detecting R-peaks in electrocardiogram (ECG) signal. *Biomedical Signal Processing and Control*, *7*(2), 118–128. https://doi.org/10.1016/j.bspc.2011.03.004

Marmarelis, V. Z. (2004). Appendix II: Gaussian White Noise. In *Nonlinear Dynamic Modeling of Physiological Systems* (pp. 499–501). John Wiley & Sons, Ltd. https://doi.org/10.1002/9780471679370.app2

Metghalchi, M., Marcucci, J., & Chang, Y.-H. (2012). Are moving average trading rules profitable? Evidence from the European stock markets. *Applied Economics*, *44*(12), 1539–1559. https://doi.org/10.1080/00036846.2010.543084

Mok, J., Mindrinos, M. N., Davis, R. W., & Javanmard, M. (2014). Digital microfluidic assay for protein detection. *Proceedings of the National Academy of Sciences*, *111*(6), 2110–2115. https://doi.org/10.1073/pnas.1323998111

Montes-Cebrián, Y., Álvarez-Carulla, A., Colomer-Farrarons, J., Puig-Vidal, M., & Miribel-Català, P. L. (2019). Self-Powered Portable Electronic Reader for Point-of-Care Amperometric Measurements. *Sensors*, *19*(17), 3715. https://doi.org/10.3390/s19173715

Norton, C. B., Wagner, K., & Hassan, U. (2019). Magnetic Phagocyte Quantification Framework for Point-of-Care Diagnostics. *2019 IEEE Healthcare Innovations and Point of Care Technologies, (HI-POCT)*, 131–134. https://doi.org/10.1109/HI-POCT45284.2019.8962692

Panneer Selvam, A., & Prasad, S. (2017). Companion and Point-of-Care Sensor System for Rapid Multiplexed Detection of a Panel of Infectious Disease Markers. *SLAS TECHNOLOGY: Translating Life Sciences Innovation*, *22*(3), 338–347. https://doi.org/10.1177/2211068217696779

Prakash, S., Ashley, B. K., Doyle, P. S., & Hassan, U. (2020). Design of a Multiplexed Analyte Biosensor using Digital Barcoded Particles and Impedance Spectroscopy. *Scientific Reports*, *10*(1), 6109. https://doi.org/10.1038/s41598-020-62894-z

Redhyka, G. G., Setiawan, D., & Soetraprawata, D. (2015). Embedded sensor fusion and moving-average filter for Inertial Measurement Unit (IMU) on the microcontroller-based stabilized platform. *2015 International Conference on Automation, Cognitive Science, Optics, Micro Electro-Mechanical System, and Information Technology (ICACOMIT)*, 72–77. https://doi.org/10.1109/ICACOMIT.2015.7440178

Saleh, O. A., & Sohn, L. L. (2003). Direct detection of antibody–antigen binding using an on-chip artificial pore. *Proceedings of the National Academy of Sciences of the United States of America*, *100*(3), 820–824. https://doi.org/10.1073/pnas.0337563100

Shi, H., Zhang, H., Ma, L., Rogers, F., Zhao, X., & Zeng, L. (2021). An Impedance Debris Sensor Based on a High-Gradient Magnetic Field for High Sensitivity and High Throughput. *IEEE Transactions on Industrial Electronics*, *68*(6), 5376–5384. https://doi.org/10.1109/TIE.2020.2988237

Stupin, D. D., Koniakhin, S. V., Verlov, N. A., & Dubina, M. V. (2017). Adaptive Filtering to Enhance Noise Immunity of Impedance and Admittance Spectroscopy: Comparison with Fourier Transformation. *Physical Review Applied*, *7*(5), 054024. https://doi.org/10.1103/PhysRevApplied.7.054024

Sui, J., Xie, P., Lin, Z., & Javanmard, M. (2020). Electronic classification of barcoded particles for multiplexed detection using supervised machine learning analysis. *Talanta*, *215*, 120791. https://doi.org/10.1016/j.talanta.2020.120791

Sukor, J. A., Redmond, S. J., & Lovell, N. H. (2011). Signal quality measures for pulse oximetry through waveform morphology analysis. *Physiological Measurement*, *32*(3), 369–384. https://doi.org/10.1088/0967-3334/32/3/008

Sun, A., Wambach, T., Venkatesh, A. G., & Hall, D. A. (2014). A low-cost smartphone-based electrochemical biosensor for point-of-care diagnostics. *2014 IEEE Biomedical Circuits and Systems Conference (BioCAS) Proceedings*, 312–315. https://doi.org/10.1109/BioCAS.2014.6981725

Sun, T., Holmes, D., Gawad, S., G. Green, N., & Morgan, H. (2007). High speed multi-frequency impedance analysis of single particles in a microfluidic cytometer using maximum length sequences. *Lab on a Chip*, *7*(8), 1034–1040. https://doi.org/10.1039/B703546B

Talukder, N., Furniturewalla, A., Le, T., Chan, M., Hirday, S., Cao, X., Xie, P., Lin, Z., Gholizadeh, A., Orbine, S., & Javanmard, M. (2017). A portable battery powered microfluidic impedance cytometer with smartphone readout: Towards personal health monitoring. *Biomedical Microdevices*, *19*(2), 36. https://doi.org/10.1007/s10544-017-0161-8

Teass, H. A., Byrnes, J., & Valentine, A. (1998). Correlation of yeast measurement: Between spin-down and Coulter Counter laboratory analysis and in-lin measurements with the McNab Cell Counter. *Technical Quarterly - Master Brewers Association of the Americas*, *35*(2), 101–103. http://pascal-francis.inist.fr/vibad/index.php?action=getRecordDetail&idt=2361471

Thompson, A. R., Stotler, R. L., Macpherson, G. L., & Liu, G. (2015). Laboratory Study of Low-Flow Rates on Clogging Processes for Application to Small-Diameter Injection Wells. *Water Resources Management*, *29*(14), 5171–5184. https://doi.org/10.1007/s11269-015-1111-y

Vandewalle, N., Ausloos, M., & Boveroux, P. (1999). The moving averages demystified. *Physica A: Statistical Mechanics and Its Applications*, *269*(1), 170–176. https://doi.org/10.1016/S0378-4371(99)00090-4

Wang, H., Sobahi, N., & Han, A. (2017). Impedance spectroscopy-based cell/particle position detection in microfluidic systems. *Lab on a Chip*, *17*(7), 1264–1269. https://doi.org/10.1039/C6LC01223J

Watkins, N. N., Hassan, U., Damhorst, G., Ni, H., Vaid, A., Rodriguez, W., & Bashir, R. (2013). Microfluidic CD4+ and CD8+ T Lymphocyte Counters for Point-of-Care HIV Diagnostics Using Whole Blood. *Science Translational Medicine*, *5*(214), 214ra170-214ra170. https://doi.org/10.1126/scitranslmed.3006870

Weissman, M. B. (1988). 1 f noise and other slow, nonexponential kinetics in condensed matter. *Reviews of Modern Physics*, *60*(2), 537–571. https://doi.org/10.1103/RevModPhys.60.537

Xu, J., Kang, J., Wang, D., Qin, Q., Liu, G., Lin, Z., Pavlovic, M., & Dostalek, P. (2016). Mathematical Model for Assessing Wort Filtration Performance Based on Granularity Analysis. *Journal of the American Society of Brewing Chemists*, *74*(3), 191–199. https://doi.org/10.1094/ASBCJ-2016-3706-01

Yeh, E.-C., Fu, C.-C., Hu, L., Thakur, R., Feng, J., & Lee, L. P. (2017). Self-powered integrated microfluidic point-of-care low-cost enabling (SIMPLE) chip. *Science Advances*, *3*(3), e1501645. https://doi.org/10.1126/sciadv.1501645

Zhang, H., Shi, H., Li, W., Ma, L., Zhao, X., Xu, Z., Wang, C., Xie, Y., & Zhang, Y. (2021). A Novel Impedance Micro-Sensor for Metal Debris Monitoring of Hydraulic Oil. *Micromachines*, *12*(2), 150. https://doi.org/10.3390/mi12020150

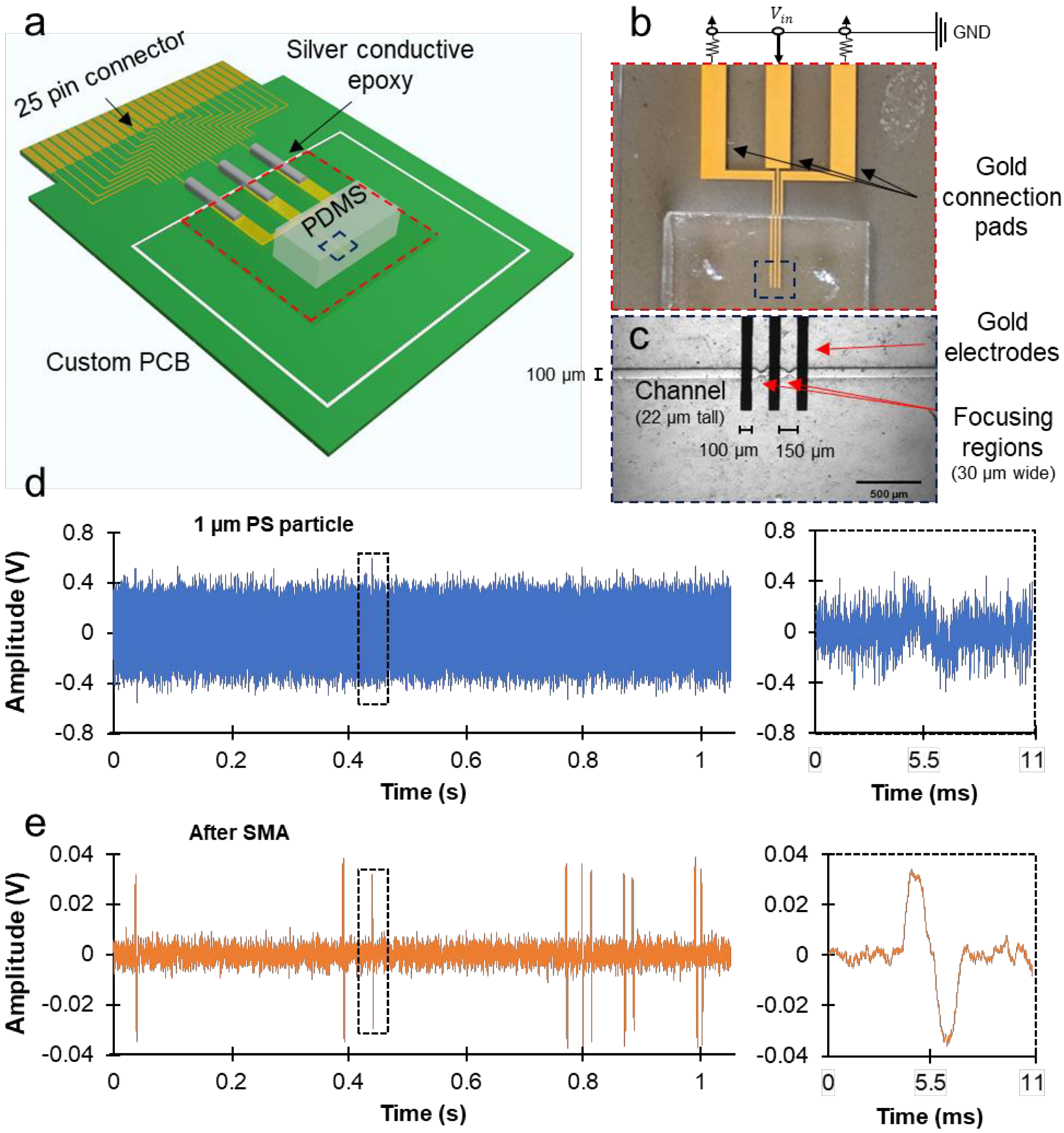

Figure 1 Overview of microfluidic impedance cytometry system. a) Scheme of custom printed circuit board (PCB) that onboards microfabricated electrodes and polydimethylsiloxane (PDMS) channel. b) Image of microfabricated gold electrodes. Middle electrode is stimulated with voltage input while two exterior electrodes are grounded for impedance detection over the generated electric field. c) Brightfield microscope image of channel detection area with focusing

regions aligned between electrodes. d) Representative results for 1 µm polystyrene (PS) particles in solution flowing through device after data processing. e) Results for the same dataset after applying a simple moving average (SMA) which averages every 100 data points and reduces background noise.

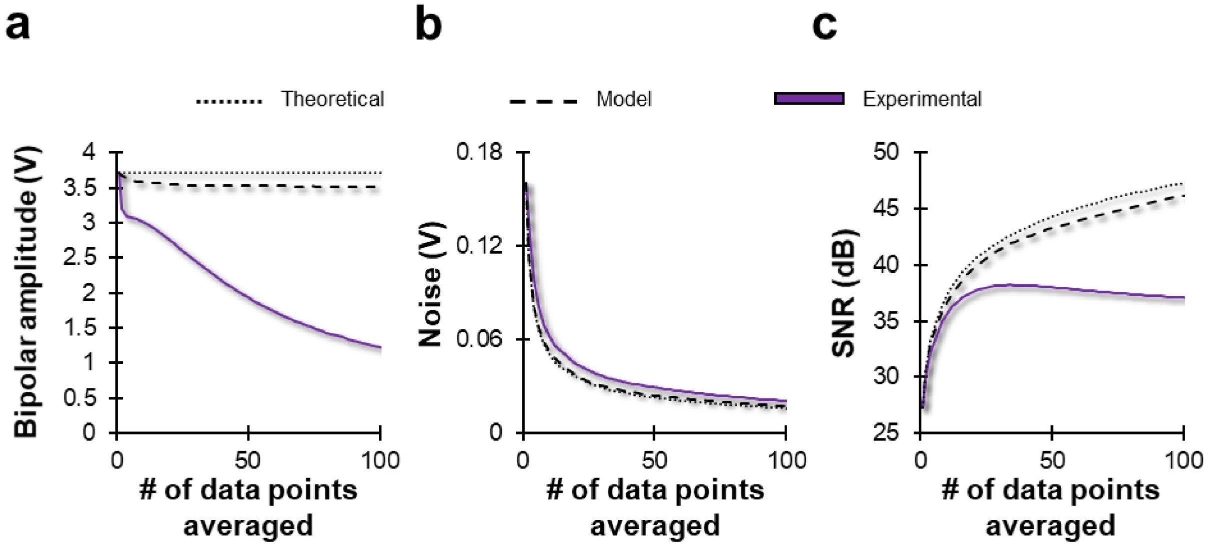

Figure 2 Representative changes in bipolar amplitude (a), noise (b), and signal-to-noise ratio (SNR) (c) as the number of signals averaged for a dataset increases. Datasets include theoretical parameters starting with the initial amplitude and noise from experimental data (dotted line), our Gaussian noise with sine wave model (dashed line) and from experimental results (data is from 9 µm polystyrene (PS) particles with a 5V input and 15 µL/min flow rate).

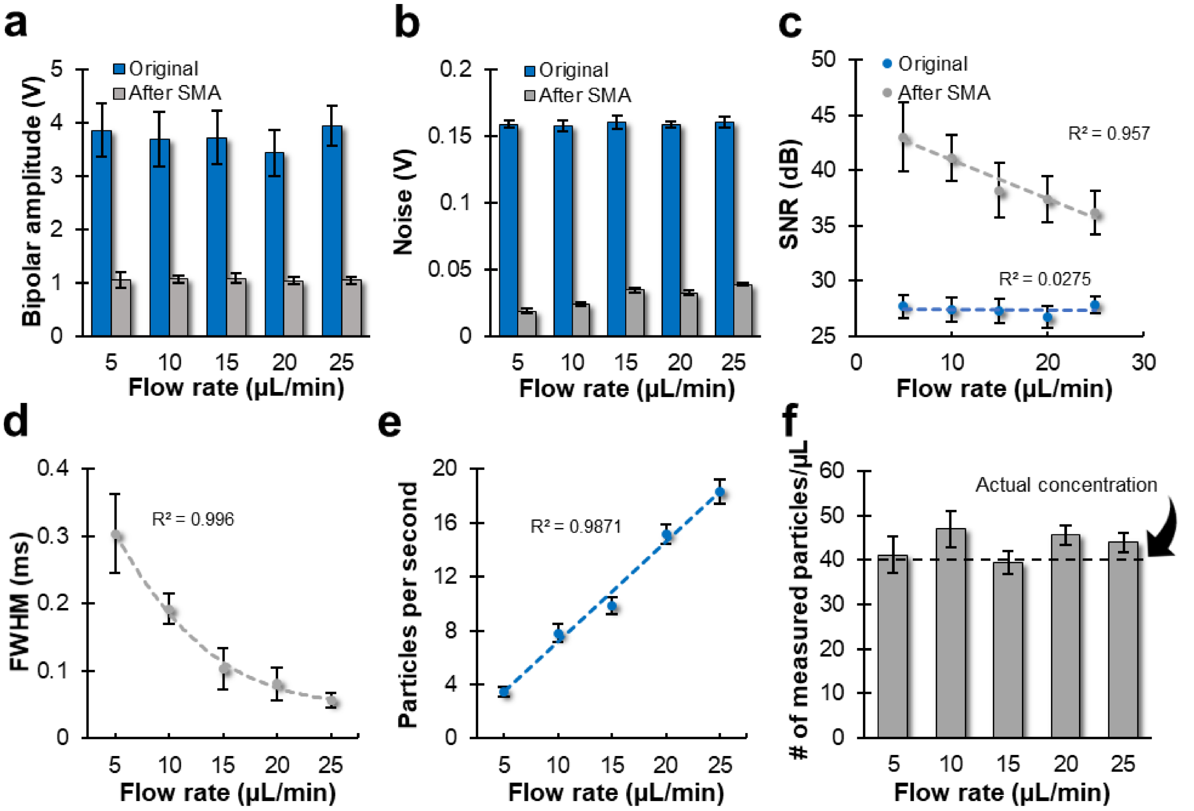

Figure 3 Results with flow rate variations and after simple moving average (SMA) effects. Changes in average bipolar amplitude (a), noise amplitude (b), and signal-to-noise ratio (SNR, c) for detecting 9 µm polystyrene (PS) particles with 5V input before (blue) and after (gray) SMA. d) Average full-width half maximum (FWHM) times for detect PS particles with varying flow rates (d-f, for original data without SMA) which follows an exponential decrease with flow rate. e) Average number of PS particles detected per second with constant particle concentration between experiments. f) Particle concentration calculated from each experiment based on total particles counted and respective flow rates, compared against the known solution concentration of 40 particles/µL (d-f, for original data without SMA). Fitted lines: Figure 4 (c) Original $y = -0.0090x + 27.53$, After SMA $y = -0.35x + 44.46$, Figure 4 (d) $y = -0.0022x^3 + 0.037x^2 – 0.21x + 0.49$, Figure 5 (e) $y = 3.71x – 0.21$.

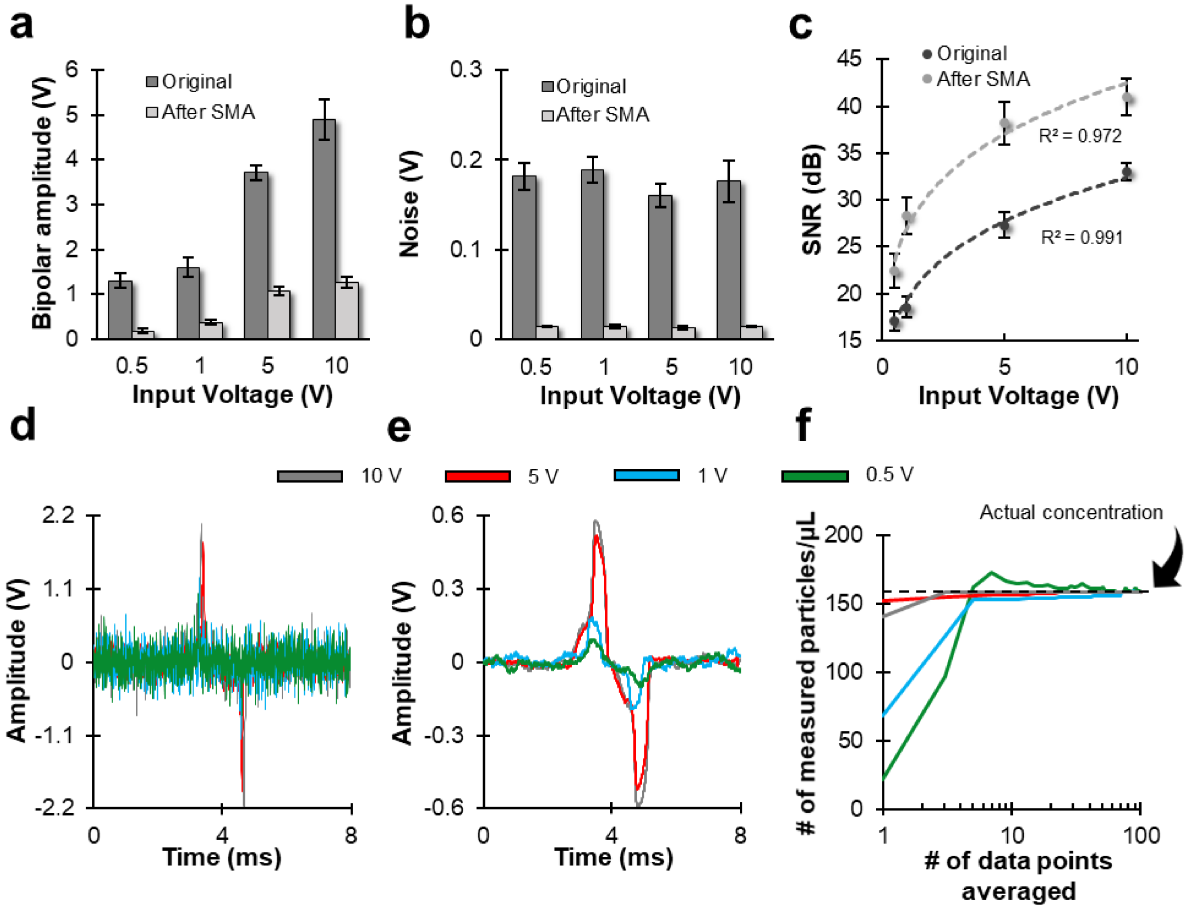

Figure 4 Results with input voltage variations and after simple moving average (SMA) effects. Changes in average bipolar amplitude (a), noise amplitude (b), and signal-to-noise ratio (SNR, c) for detecting 9 µm polystyrene (PS) particles with 15 µL/min flow rate before (dark gray) and after (light gray) SMA. Example PS pulses before (d) and after (e) SMA for different voltage inputs. (f) Semi-log plot showing changes in measured number of particles from the counter after increasing iterations of signal averaging compared to the stock concentration of 160 particles/µL (black dotted line). Fitted lines: Figure 4 (c) Original $y = 19.33x^{0.22}$, After SMA $y = 26.95x^{0.198}$.

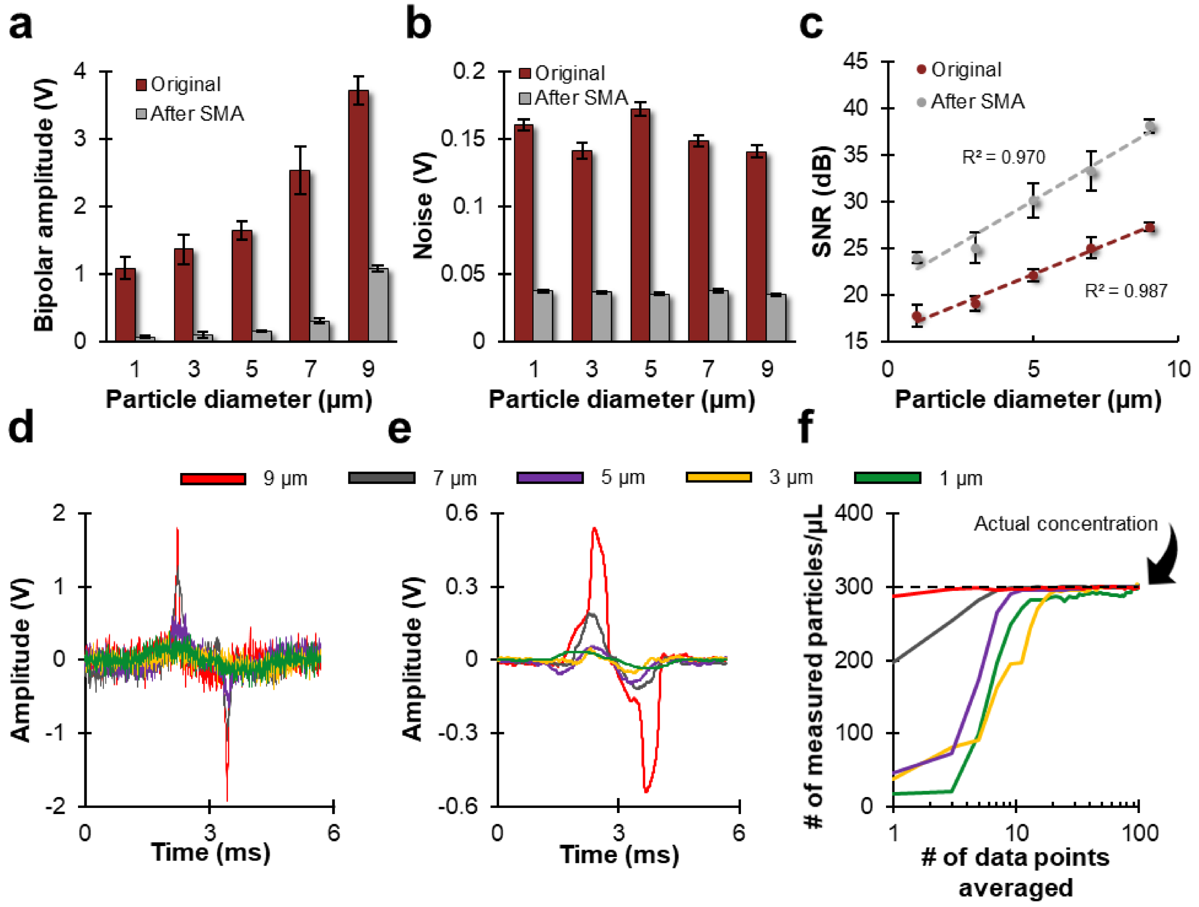

Figure 5 Results with polystyrene (PS) particle size variations and after simple moving average (SMA) effects. Changes in average bipolar amplitude (a), noise amplitude (b), and signal-to-noise ratio (SNR, c) for detecting PS particles with 5V input and 15 µL/min flow rate before (maroon) and after (gray) SMA. Example PS pulses before (d) and after (e) SMA for different PS particle sizes. (f) Semi-log plot showing changes in measured number of particles from the counter after increasing iterations of signal averaging compared to the stock concentration of 300 particles/µL (black dotted line). Fitted lines: Figure 5 (c) Original $y = 1.25x + 16.03$, After SMA $y = 1.82x+21.02$.